

Cluster infall in the concordance Λ -CDM model.

Maximiliano C. Pivato¹, Nelson D. Padilla^{1,2} and Diego G. Lambas^{1,3}

¹ *Grupo de Investigaciones en Astronomía Teórica y Experimental (IATE), Observatorio Astronómico Córdoba, UNC, Argentina.*

² *Departamento de Astronomía y Astrofísica, Pontificia Universidad Católica, V. Mackenna 4860, Santiago 22, Chile.*

³ *Consejo Nacional de Investigaciones Científicas y Tecnológicas (CONICET), Argentina.*

Accepted ??? Month ?. Received ??? Month ??

ABSTRACT

We perform statistical analyses of the infall of dark-matter onto clusters in numerical simulations within the concordance Λ CDM model. By studying the infall profile around clusters of different mass, we find a linear relation between the mass and maximum infall velocities which reach ~ 900 km/s for the most massive groups. The maximum infall velocity and the group mass follow a suitable power law fit of the form, $V_{inf}^{max} = (M/m_0)^\gamma$. By comparing the measured infall velocity to the linear infall model with an exponential cutoff introduced by Croft et al., we find that the best agreement is obtained for a critical overdensity $\delta_c = 45$. We study the dependence of the direction of infall with respect to the cluster centres, and find that in the case of massive groups, the maximum alignment occurs at scales $r \sim 6h^{-1}$ Mpc. We obtain a logarithmic power-law relation between the average *infall angle* and the group mass. We also study the dependence of the results on the local dark-matter density, finding a remarkable difference in the dynamical behaviour of low- and high-density particles.

Key words: Cosmology: Velocity Field – Large Scale Structure of the Universe

1 INTRODUCTION

The large-scale velocity field provides a significant source of information on the distribution of mass fluctuations in the Universe. Moreover, the relation between peculiar velocities and mass is simple, providing a direct indication of the distribution of mass independent of assumptions about the bias factor of different galaxy types.

Large scales flows have been addressed both theoretically (Regös & Geller 1989, Bothun et al. 1990, Hiotelis 2001) and observationally (Dekel 1999, Cecarrelli et al. 2005, for a review see Strauss & Willick 1995). On the other hand, the dynamical behavior of objects near regions of high density contrast can be described by the spherical infall model (Regös & Geller 1989) with a collapsing streaming motion whose amplitude depends only on the distance to the local density maximum (Diaferio & Geller 1997). The predictions from the spherical infall model are often used for cluster mass estimates (*e.g.* Diaferio 1999). Gunn (1978) and Peebles (1976, 1980) derived a linear approximation to the infall velocity induced by an isotropic mass concentration described by $\delta(r) = \rho(r)/\rho_b - 1$, where $\rho(r)$ is the average density inside a radius r and ρ_b is the background density. The infall velocity V_{inf} is then given by

$$V_{inf}^{lin} = -\frac{1}{3}H_0\Omega_0^{0.6}r\delta(r), \quad (1)$$

where H_0 is the Hubble constant and Ω_0 is the cosmolog-

ical density parameter. Yahil (1985) provides a non-linear approximation to the exact solution of the infall velocity:

$$V_{inf}^{non-lin} = -\frac{1}{3}H_0\Omega_0^{0.6}r\frac{\delta(r)}{[1+\delta(r)]^{0.25}}; \quad (2)$$

however, this equation is not accompanied by a published derivation. Regös & Geller (1989), assume that clusters are spherically symmetric and obtain a solution for the non-linear infall velocity of the system as an expansion series, which is accurate before orbit crossing takes place and for $\delta < 1 - 2$. They also quote that this solution is inadequate for large density enhancements. Therefore, neither their calculations nor Eqs. 1 or 2, are expected to hold in or near cluster centres, or more generally in virialised regions. In order to overcome this problem, Croft, Dalton & Efstathiou (1999) -hereafter, CDE- choose to truncate the expression for $V_{inf}^{non-lin}$ with an exponential cutoff $e^{-\delta(r)/\delta_c}$ with $\delta_c = 50$, which roughly approximates the effect of the rapid decrease of infall velocities at small r due to virialised motions (see figure 7 in CDE). When adding the exponential cutoff, the expression for the linear infall velocity given by Eq. 1 becomes:

$$V_{inf}^{lin} = -\frac{1}{3}H_0\Omega_0^{0.6}r\delta(r)e^{\delta(r)/\delta_c}; \quad (3)$$

for the non-linear infall velocity (Eq. 2) this is:

$$V_{inf}^{non-lin} = -\frac{1}{3}H_0\Omega_0^{0.6}r\frac{\delta(r)e^{-\delta(r)/\delta_c}}{[1+\delta(r)]^{0.25}}. \quad (4)$$

CDE claim to obtain a better fit to their simulations using this equation, but given the arbitrary nature of this truncation, they still restrict their analysis to the outer regions of haloes ($r > 2.5h^{-1}$ Mpc).

In this paper, we explore the characteristics of streaming motions in the regions surrounding clusters using large, high resolution VIRGO N-body simulations, and compare these results to predictions from linear theory and the spherical infall model. We will also study the alignments between the velocity field and the positions of haloes in the numerical simulation, to determine the extent to which a radial approximation to the velocity field around high-density peaks is valid. In a related subject, we will provide a further quantification of velocity alignments by measuring the fractions of particles flowing towards haloes with respect to those staying at roughly fixed gravitational potentials, and we will compare it to the fraction of particles escaping the potential wells of haloes. In all these analyses we will also study the impact of local density on the infall and alignment of motion towards clusters.

This paper is organised as follows: Section 2 contains a brief description of the numerical simulations used in this work; Section 3 describes the statistical analyses and the resulting dependencies of the infall pattern on cluster mass and local density. Finally, Section 4 contains a summary of the conclusions drawn from this work.

2 NUMERICAL SIMULATIONS

The numerical simulation used in this work was carried out by the Virgo Consortium. In particular, we use the publicly available Very Large Simulations, VLS (Yoshida et al. 2001), characterised by a Λ CDM model, 512^3 particles in a cosmological box of $480h^{-1}$ Mpc on a side, and a mass resolution of $6.86 \times 10^{10}h^{-1}M_\odot$. The cosmology is characterised by a matter density parameter $\Omega_0 = 0.3$, cosmological constant $\Omega_\Lambda = 0.7$ and expansion rate at the present time $H_0 = 100h$ Mpc km/s where $h = 0.7$. The Cold Dark Matter (CDM) initial power spectrum was computed using the *CMBFAST* software (Seljak & Zaldarriaga 1996), and is normalised to the abundance of galaxy clusters at $z = 0$ so that $\sigma_8 = 0.9$. Dark-matter haloes are identified in the simulation using a standard *friends-of-friends* algorithm (Davis et al. 1985) using a linking length l , given by $l = 0.17\bar{n}^{-1/3}$, where \bar{n} is the mean number density of particles; this linking length corresponds to an overdensity $\delta\rho/\rho \simeq 200$, which characterises the virialized halo and separates it from the surrounding infall material (Cole & Lacey 1995). This large simulation contains a large number of halos spanning a wide range of masses. The criteria followed in the identification of dark-matter haloes leads to $\sim 720,000$ identified systems with masses ranging from $6.8 \times 10^{11}h^{-1}M_\odot$ (10 particles) to $2.35 \times 10^{15}h^{-1}M_\odot$ (more than 20,000 particles).

In Figure 1 we plot a slice of the VLS simulations where the distribution of particles is shown in a logarithmic gray-scale density plot. The dark matter density was smoothed using a $R = 1h^{-1}$ Mpc top-hat filter and corresponds to a slice of $60h^{-1}$ Mpc a side and $10h^{-1}$ Mpc deep. The black arrows indicate the projected velocity field of 20% of the

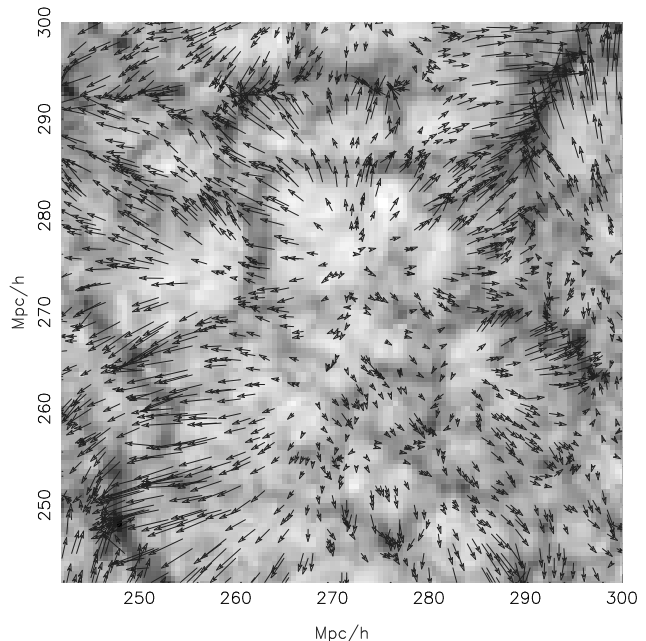


Figure 1. Infall pattern in a slice, $60h^{-1}$ Mpc a side and $10h^{-1}$ Mpc thick, of the VLS simulation box. The particle density is plotted in a logarithmic gray-scale, smoothed using a top-hat function ($R = 1h^{-1}$ Mpc). The black solid arrows show the peculiar velocity field.

particles in the slice. It can be clearly appreciated the systematic infall flow onto dense regions, as well as outflow patterns from the lower density regions.

We calculate the halo peculiar velocity by averaging the individual group member velocities. In Figure 2 we show the normalised distribution function of the peculiar velocity of halos with masses between $10^{11}h^{-1}M_\odot - 10^{12}h^{-1}M_\odot$ (dotted line), $10^{12}h^{-1}M_\odot - 10^{13}h^{-1}M_\odot$ (short dashed line), $10^{13}h^{-1}M_\odot - 10^{14}h^{-1}M_\odot$ (long dashed line) and more than $10^{14}h^{-1}M_\odot$ (solid line); and the distribution function of peculiar velocities of the dark matter particles (thick short-dashed line). As can be seen, even the most massive groups have similar mean-velocities than dark-matter particles (Einasto et al. 2005, Shaw et al. 2005). However, only dark-matter particles show a high velocity tail ($\mathbf{V} > 1500$ km/s), whereas groups rarely reach peculiar velocity values above $\mathbf{V} = 1000$ km/s (Shaw et al. 2005).

3 VELOCITY FIELD ANALYSIS

In this section we study the statistical properties of the velocity field in the neighborhoods of dark-matter haloes, up to scales of $40h^{-1}$ Mpc. We begin by analysing the mean infall velocity of particles onto groups, and the distribution of the peculiar velocity orientation of the particles in the outskirts of the groups (Subsection 3.1). In Subsection 3.2 we study the dependence of the results on the local dark-matter density. We perform our analysis for four different group mass samples (see Table 1).

All our analyses are performed using individual particles in the simulation as opposed to the recent use of sub-structure identified in simulations in several works (see for

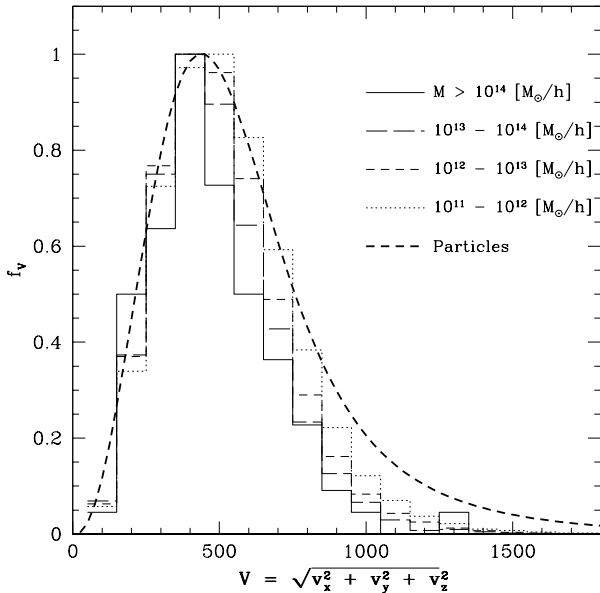


Figure 2. Normalised distribution function, f_v , of the velocity module $\mathbf{V} = \sqrt{v_x^2 + v_y^2 + v_z^2}$ for particles (thick short dashed line) and groups with masses in the ranges $10^{11}h^{-1}M_\odot - 10^{12}h^{-1}M_\odot$ (dotted line), $10^{12}h^{-1}M_\odot - 10^{13}h^{-1}M_\odot$ (short dashed line), $10^{13}h^{-1}M_\odot - 10^{14}h^{-1}M_\odot$ (long dashed) and more than $10^{14}h^{-1}M_\odot$ (solid line).

Table 1. Description of our samples of dark-matter haloes corresponding to different ranges of mass and the number of groups identified.

Sample	Mass interval [$h^{-1}M_\odot$]	Number of groups
S1	$3.4 \times 10^{12} - 6.8 \times 10^{12}$	73509
S2	$6.8 \times 10^{12} - 6.8 \times 10^{13}$	72465
S3	$6.8 \times 10^{13} - 6.8 \times 10^{14}$	6097
S4	$> 6.8 \times 10^{14}$	92

instance Benson, 2005, and Wang et al., 2005). We consider that our studies should not change importantly if we were to repeat the following analyses using substructure since we are particularly interested in regions outside the halo centres. At such distances, we expect the average velocities of individual particles and substructure to be similar. This is opposed to the clear differences inside dark-matter haloes, where dynamical friction would slow down the center of mass of a sub-halo.

3.1 The average velocity infall

We start our analysis of the velocity field by computing the group-averaged infall velocity as follows: we select groups in a specific mass range, and calculate the mean particle infall velocity as a function of distance to the group centres. In Figure 3 we plot the mean infall velocity profile for the four subsamples S1, S2, S3 and S4 (dotted, short-dashed, long-dashed and solid line respectively) described in Table 1. As it can be seen, the maximum infall velocity, V_{infall}^{max} , increases

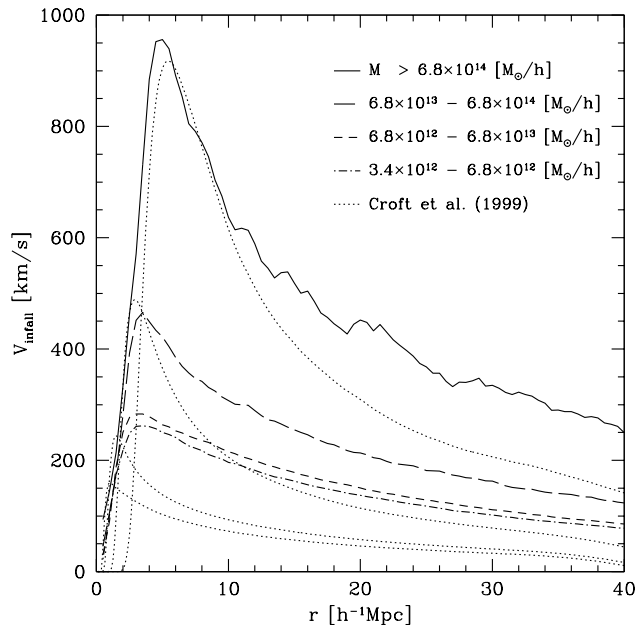


Figure 3. Average infall velocity onto groups in samples S1, S2, S3 and S4 (dot dashed, short dashed, long dashed and solid lines, respectively) as function of scale. Dotted lines represent the results from the linear fit with an exponential cutoff (Eq. 3) with $\delta_c = 50$.

with the group mass, with values $V_{infall}^{max} \sim 250$ km/s for groups in sample S1, and $V_{infall}^{max} = 950$ km/s for those in S4, the most massive groups in our analysis. The rapid decrease of infall velocities at small scales indicates the boundary of the virialised region. It can also be seen that the scale of the maximum infall velocity correlates well with group mass, a somewhat expected effect given the correlation between mass and virial radius. We notice a more rapid decrease of the infall pattern for the most massive groups compared to the gentle decline shown by low mass systems. We compare the actual infall velocity measured in the simulations with the prediction from the CDE model. In order to do this, we calculate the averaged density enhancement inside a sphere of radius r centered in each group and derive the linear infall velocity using an exponential cutoff given by Eq. 3 for the same mass intervals described in Table 1. The results are plotted in Figure 3, where it can be appreciated that although this model provides a reasonable agreement to the infall around high mass haloes, there are still large discrepancies at small and large scales, specially for the lower mass ranges explored here.

The results shown in Figure 3 indicate a tight relation between V_{infall}^{max} and group mass in both, the patterns measured in the simulations, and the results from Eq. 3. In order to address the infall correlation with group mass we measure the mean infall profile for different mass ranges, and compute V_{infall}^{max} . In Figure 4, we show the maximum mean infall velocity as a function of group mass in the simulation (solid circles), and from Eq. 3 (open triangles).

A suitable power-law fit to the simulation results is:

$$V_{infall}^{max} = \left(\frac{M}{m_0}\right)^\gamma, \quad (5)$$

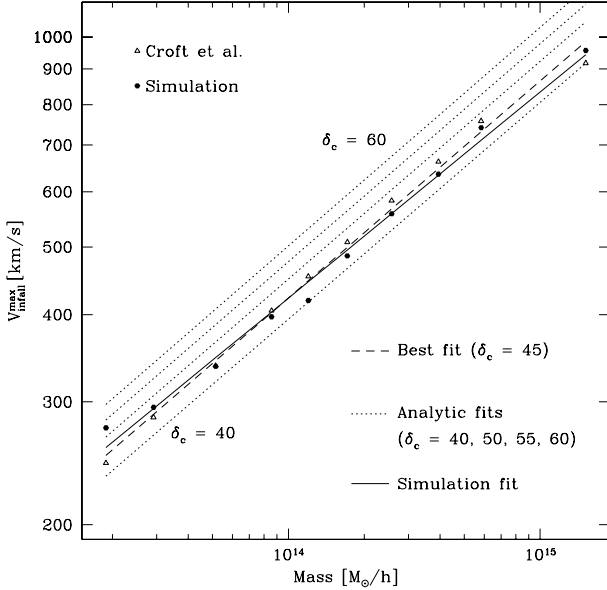


Figure 4. Maximum infall velocity as a function of group mass measured in the simulation (black dots) and its corresponding power-law fit (solid line). The open triangles show the same relation as obtained from the maxima in Eq. 3. We also show for comparison the results from Eq. 7, assuming different values of $\delta_c = 40, 45, 50, 55, 60$ (dotted lines). The best-fit to the simulation results is given by the dashed line, which corresponds to $\delta_c = 45$.

where the parameter values are $m_0 = 1.29 \times 10^5$, and $\gamma = 0.29$. Using the linear fit with the exponential cutoff given by Eq. 3, it is possible to infer a relation between the scale of the maximum infall velocity and the halo mass:

$$r_{inf}^{max} = \left(\frac{3A}{8\pi\rho_m} \right)^{1/3} M^{1/3}. \quad (6)$$

where the factor A is defined as function of δ_c as $A = \sqrt{(2 + 3/\delta_c)^2 + 12/\delta_c} - 2 - 3/\delta_c$, with $A > 0$ for any given positive value of δ_c . Replacing r by r_{inf}^{max} in Eq. 3, we find the expression for V_{inf}^{max} :

$$V_{inf}(r_{max}) = \frac{(9\pi)^{-1/3} H_0 \Omega_0^{0.6}}{2 \rho_m} \left(\frac{2-A}{A^{2/3}} \right) e^{-\frac{2-A}{A\delta_c}} M^{1/3}. \quad (7)$$

By setting $H_0 = 70$, $\Omega_m = 0.3$ and $\delta_c = 50$, we obtain $V_{inf}(r_{max}) \simeq M^{1/3}/2.25 \times 10^4$, which is very similar to our power-law fit in Eq. 5. We now calculate $V_{inf}^{max}(M)$ from Eq. 7 using different values of $\delta_c = 40, 45, 50, 55$ and 60 , and plot the results in Figure 4 (dotted lines). As it can be seen in this figure, the best fit to the simulations is achieved when using $\delta_c \sim 45$ (dashed line). The power-law behaviour of $V_{inf}^{max}(M)$ brakes down at low mass halos, when $M < 10^{13} h^{-1} M_\odot$. At this point, the maximum infall velocity does not change considerably with halo mass, as can be seen in the infall patterns for samples S1 and S2 in figure 3. The reason behind this may be related to the flattening of the bias between dark-matter haloes and mass $b(M)$, which occurs at similar mass scales; namely, the clustering around groups of masses $M < 10^{13} h^{-1} M_\odot$ can be considered to be almost independent of halo mass.

In order to characterise the alignments of the infall of

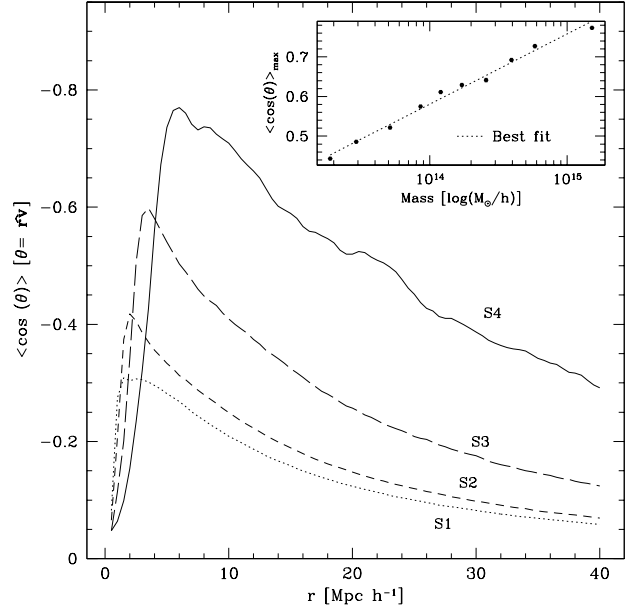


Figure 5. Average cosine of the angle between the cluster-centric position and peculiar velocity of dark-matter particles around halos in the simulation. Groups are divided into samples spanning different mass ranges indicated in Table 1 (samples S1, S2, S3 and S4, in dotted, short dashed, long dashed and solid lines, respectively). The inset shows the relation between $\langle \cos(\theta) \rangle_{max}$ and group mass. The dotted line corresponds the best log-linear fit to this relation, $\cos(\theta)_{max} = \gamma \log(M/C_0)$, where $\gamma = 0.17$ and $C_0 = 5.18 \times 10^{10}$.

dark-matter in the outskirts of haloes, we centre our origin on each halo, and measure the angle θ between the particle position vector and its peculiar velocity. In order to detect variations with the halo mass, we analyse subsamples S1, S2, S3 and S4 described in Table 1. Figure 5 shows the results from averaging $\langle \cos(\theta) \rangle$ over each sample of haloes (dotted, short dashed, long dashed and solid lines for samples S1, S2, S3 and S4, respectively).

Dark-matter particles infalling towards S4 groups show the maximum alignment, $\cos(\theta)_{max} \simeq -0.77$ at $r \simeq 5.5 h^{-1}$ Mpc. In contrast, the peculiar velocity of particles in the outskirts of groups in sample S1 show the lowest alignment, with $\cos(\theta)_{max} \simeq -0.3$ at $r \simeq 1 h^{-1}$ Mpc. As can be seen, we obtain a maximum ‘coherence’ for the alignment in a relatively small range of scales: $1 h^{-1}$ Mpc $\lesssim r \lesssim 6 h^{-1}$ Mpc. The velocity field of the particles around the most massive groups (sample S4) show a significant alignment at large scales ($r > 30 h^{-1}$ Mpc). However, for less massive systems, $\langle \cos(\theta) \rangle$ is significantly reduced. It can also be appreciated that the maximum alignment between the cluster-centric position and the peculiar velocity of the particles is a function of group mass. We show this relation in the inset of Figure 5 for different masses (same samples as those in Figure 4). An empirical logarithmic power-law fit,

$$\cos(\theta)_{max}(M) = \gamma \log(M/C_0), \quad (8)$$

with parameters $\gamma = 0.17$ and $C_0 = 5.18 \times 10^{10}$, gives a very good agreement to the simulation results, as can be seen in dotted line in the inset of Figure 5.

We perform a further study of the *infall-angle* in the

outskirts of dark-matter haloes by comparing the number of particles in each shell of radius r with peculiar velocities pointing outwards from the group center, to the number pointing towards the group center. We measure $N_i(r)$, $N_m(r)$ and $N_o(r)$, which indicate the number of particles characterised by $1/3 \lesssim \cos(\theta)$ (infall), $-1/3 < \cos(\theta) < 1/3$ (intermediate) and $\cos(\theta) \lesssim -1/3$ (outflow), respectively, at a distance r from the group centre. We average across our sample, and calculate the ratios $D_i(r) = \langle (N_i(r)/N_m(r)) \rangle$ and $D_o(r) = \langle (N_o(r)/N_m(r)) \rangle$. Figure 6 show the results for $D_i(r)$ (thick lines) and $D_o(r)$ (thin lines) for the samples S1, S2, S3 and S4 (dotted, short-dashed, long-dashed and solid lines, respectively). As can be seen, samples S1 and S2 show $D_o > 1$ at $r > 30h^{-1}$ Mpc, indicating that the large density inhomogeneities marked by the halo centres are still correlated with the distribution of mass at such large distances.

The fact that the maximum of D_i and minimum of D_o coincide with one another, as well as with the maximum alignment as measured by $\cos(\theta)$, is to be expected since the maximum alignment occurs when the fraction of infalling particles reaches its maximum (compare figure 5 and 6). We also notice that these maxima occur at larger distances for higher mass haloes, consistent with the maximum infall velocities occurring further away from the most massive haloes. We notice that the maximum infall velocity occurs $\sim 30\%$ closer to the group than the maximum velocity alignment. This suggests that alignments are a better choice than infall velocities for the determination of the distance where the halo virialisation breaks the trend of increasing infall and velocity alignments toward the halo centres. In general, our results are consistent with high mass haloes being more relaxed systems with isotropic velocity distributions.

3.2 The infall dependence on local density.

In this subsection, we analyse the dependence of the infall pattern, the *infall-angle* and the parameters D_i and D_o on the local density of the dark-matter particle being considered in the analysis. We define a local number density, ρ_n , as the number of particles in cubic cells of side $l_c = 3h^{-1}$ Mpc (note this is not a proper density definition, just a simple parameter to characterise the environment of a dark-matter particle), and a mean numerical density, $\bar{\rho}_n$, as the mean number of particles expected in cells of volume $V_c = l_c^3$ (in this particular numerical simulation, and for the chosen value of l_c , the mean numerical density is $\bar{\rho}_n = 33$). All particles within a cubical cell are assigned the same density and we divide our analysis according to the following ranges of local density: *high*, *intermediate* and *low densities* defined as $\rho_n/\bar{\rho}_n > 2$, $1/2 < \rho_n/\bar{\rho}_n < 2$ and $\rho_n/\bar{\rho}_n < 1/2$, respectively.

In order to test the possibility of a further dependence of the infall pattern on mass and local density, we analysed the fraction of particles laying in different density ranges as function of scale. The fraction of particles in high, intermediate and low density regions are calculated using $f_{hi} = N_{hi}/N_{tot}$, $f_{av} = N_{av}/N_{tot}$ and $f_{lo} = N_{lo}/N_{tot}$, where N_{hi} , N_{av} and N_{lo} are the number of particles in high, intermediate and low density regions respectively, and $N_{tot} = N_{hi} + N_{av} + N_{lo}$ is the total number of particles within each distance interval. In figure 7 we plot with thick lines the fraction of particles f_{hi} (solid lines), f_{av} (dashed lines) and f_{lo} (dotted lines) for the S4 $M > 6.8 \times 10^{14}$ sample, and with thin lines the corre-

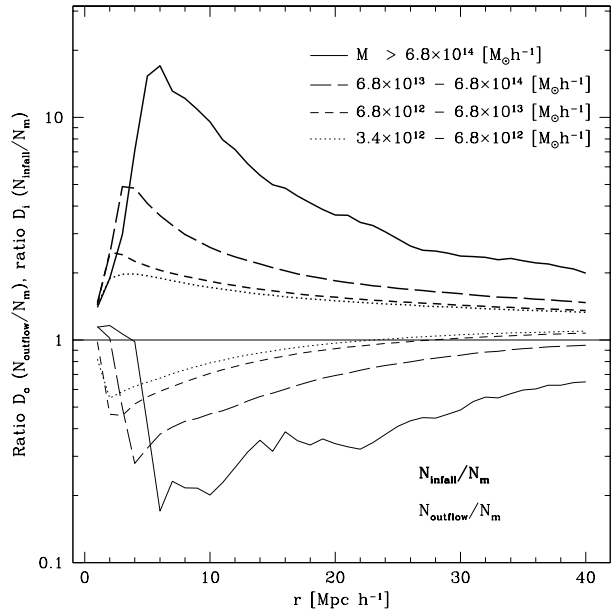


Figure 6. The average ratio between the number of particles with $1/3 < \cos(\theta) < 1$ ($N_{outflow}$) and $-1/3 < \cos(\theta) < 1/3$ (N_m), referred to as D_i (black); and the ratio between the number of particles with $-1 < \cos(\theta) < -1/3$ (N_{infall}) and N_m , referred to as D_o (red). These ratios are plotted for the different mass ranges used in previous plots: $3.45 \times 10^{11} - 6.8 \times 10^{12} h^{-1} M_\odot$ (dotted line), $6.8 \times 10^{12} - 6.8 \times 10^{13} h^{-1} M_\odot$ (short dashed line), $6.8 \times 10^{13} - 6.8 \times 10^{14} h^{-1} M_\odot$ (long dashed line) and $M > 6.8 \times 10^{14} h^{-1} M_\odot$ (solid line).

sponding fraction of particles for sample S1 ($M < 6.8 \times 10^{12}$). In this figure, we can appreciate that the infall patterns corresponding to f_{hi} for the two mass range sample differ in less than 20% in scales $r < 20Mpc/h$ while the patterns of f_{av} and f_{lo} are similar within 10% in the same scales.

In Figure 8 we plot the average infall velocity of particles with $\rho/\bar{\rho} > 2$ (solid lines), $\rho/\bar{\rho} \sim 1$ (dashed lines) and $\rho/\bar{\rho} < 1/2$ (dotted lines) as a function of the scale, for the four group samples S1, S2, S3 and S4 (panels A, B, C and D respectively). It can be noticed that more massive haloes tend to show less differences in the infall patterns of high and low density particles (almost no difference in panel D), whereas low mass groups (panel A) show a difference between maximum infall of high and low density particles of ~ 200 km/s (more than 60% of the maximum infall for the high density particles). We provide fits to the V_{inf}^{max} vs. mass relation for the different ranges of local density in table 2, where it can be seen that both the slope, γ , and m_0 increase for decreasing local density values. Note that the global fit is similar to that of $\rho_n > 2\bar{\rho}_n$, which indicates that the signal from high density regions dominates the overall infall velocity.

In order to get a deeper insight on the flow patterns in the outskirts of groups, we also study the dependence of the *infall-angle* on density; we compute the average $\langle \cos(\theta) \rangle$ for particles characterised by a local density ρ_n . Figure 9 shows these results for the mass samples defined in Table 1 (panels A, B, C and D for samples S1, S2, S3 and S4 respectively) for particles in high density environments, $\rho \gg \bar{\rho}$ (solid lines); intermediate densities, $\rho \sim \bar{\rho}$ (dashed

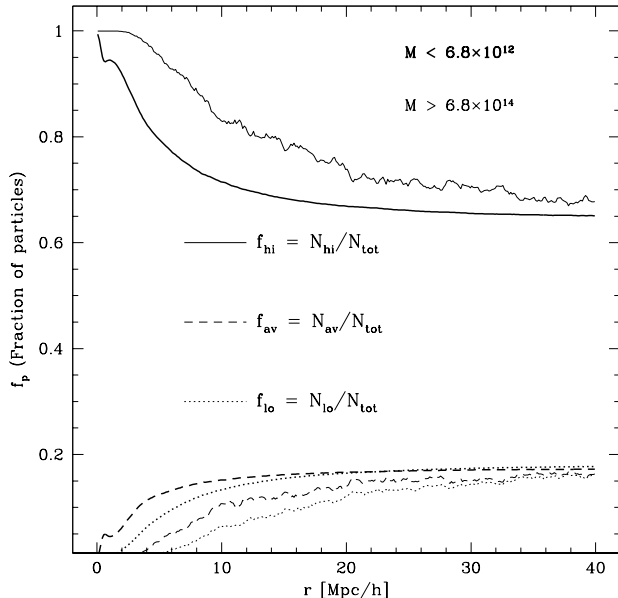


Figure 7. Fraction of particles in high, intermediate and low density regions, f_{hi} (solid lines), f_{av} (dashed lines) and f_{lo} (dotted lines), respectively as a function of scale. The thick lines correspond to the most massive groups (sample S4) and the thin lines to the least massive ones (sample S1).

Table 2. Values obtained for the parameters γ and m_0 in the fit of V_{infall}^{max} vs. mass, for different values of local density.

Local density parameter (ρ_n)	γ	m_0
All ρ_n values	0.295	1.29×10^5
$\rho_n > 2\bar{\rho}_n$	0.281	4.22×10^4
$\bar{\rho}_n/2 < \rho_n < 2\bar{\rho}_n$	0.404	4.85×10^7
$\rho_n < \bar{\rho}_n/2$	0.442	1.36×10^8

line) and low densities, $\rho < \bar{\rho}$ (dotted line). Each group sample shows different features in their alignment profiles including different maximum alignments; we notice that for higher mass groups the maximum alignment is more significant, as can be seen in Figure 5. For the least massive groups (sample S1 in panel A) we obtain a maximum alignment of $\langle \cos(\theta) \rangle \sim -0.5$ at $r \sim 3h^{-1}$ Mpc for low density particles, and a lower maximum alignment for particles in high density regions, $\langle \cos(\theta) \rangle \sim -0.25$ at $r \sim 4h^{-1}$ Mpc. However, at larger scales, $r > 6h^{-1}$ Mpc, high-density particles are better aligned than low-density particles. Samples S2 and S3 (intermediate masses) show a similar behaviour: the maximum alignment of low-density particles around groups in sample S2 reaches $\langle \cos(\theta) \rangle \sim -0.6$, whereas the high-density particles reach $\langle \cos(\theta) \rangle \sim -0.4$, both at $r > 8h^{-1}$ Mpc. As can be seen, the peculiar velocities of higher-density particles are more aligned with the direction to the centre of the halo. In the case of group sample S3 the particles in low density regions have a maximum alignment $\langle \cos(\theta) \rangle \sim -0.8$ whereas high-density particles show a maximum alignment $\langle \cos(\theta) \rangle \sim -0.6$. Again, at scales $r > 20h^{-1}$ Mpc, higher density particles are more aligned. In group sample S4 it can

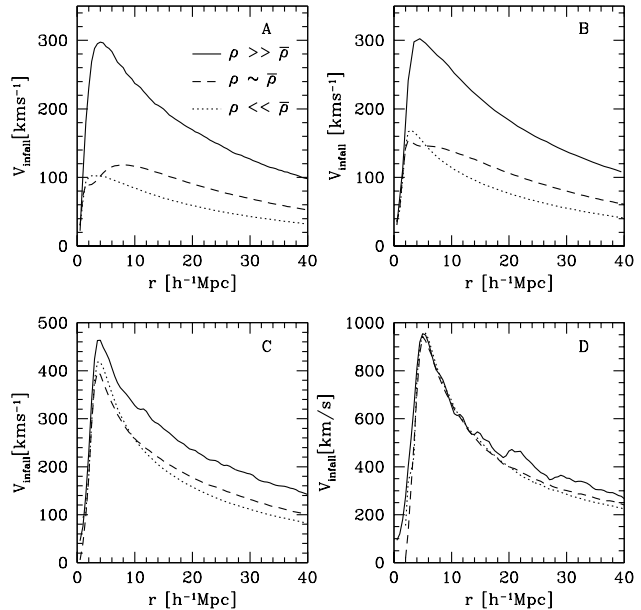


Figure 8. Mean infall velocity as a function of scale. Halo samples correspond to S1, S2, S3 and S4, and are defined in Table 1 (panels A, B, C and D). The different lines show the average infall patterns of particles in regions with density $\rho \gg \bar{\rho}$ (solid line), $\rho \sim \bar{\rho}$ (dashed line) and $\rho \ll \bar{\rho}$ (dotted line).

Table 3. Values obtained for the parameters γ and C_0 in the fit of $\cos(\theta)_{max}$ vs. mass, considering different ranges of local density.

Local density (ρ_n)	γ	C_0
All ρ_n values	0.176	5.18×10^{10}
$\rho_n > 2\bar{\rho}_n$	0.178	6.16×10^{10}
$\bar{\rho}_n/2 < \rho_n < 2\bar{\rho}_n$	0.159	2.66×10^9
$\rho_n < \bar{\rho}_n/2$	0.157	1.05×10^9

be observed that particles in low and high density environments show the same maximum alignment $\cos(\theta) \sim -0.8$ at $r \sim 6h^{-1}$ Mpc, while particles with intermediate densities are more strongly aligned, with $\cos(\theta) \sim -0.9$. For this particular group sample, we do not find a significant difference in the alignment of high, medium, and low density particles. Table 3 shows the parameter values for the fits to $\cos(\theta)_{max}$ vs. mass for the different ranges of local densities and halo mass considered here. As can be seen, both the slope γ and c_0 are larger for higher densities. This indicates that particles in denser regions are moving in a direction better aligned to the center of the groups. As in the case of the maximum infall velocity, it can also be seen that the parameter fits resulting from all the particles surrounding groups is similar to the fit from the particles in the densest regions, indicating that the latter dominate the alignment signal.

We now search for possible dependencies of the fraction of infalling and outflowing particles, D_o and D_i defined above, on the local density of dark-matter particles. Figure 10 presents these results for our four group samples (panels A, B, C and D for samples S1, S2, S3 and S4, respectively)

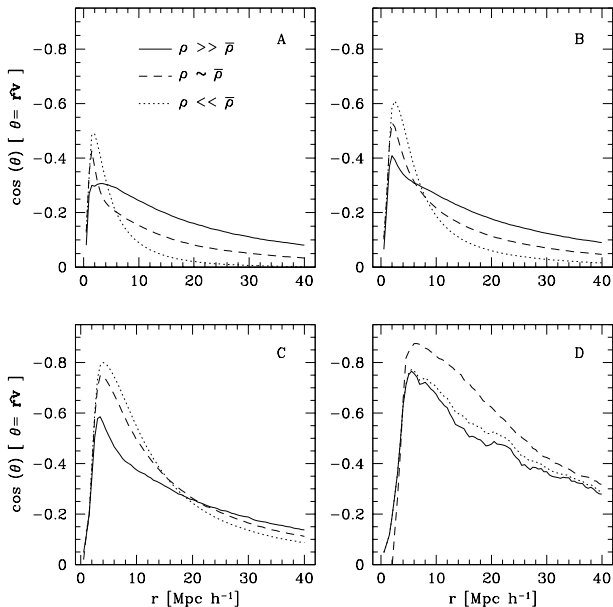


Figure 9. Dependence of $\langle \cos(\theta) \rangle$ on local density for our four mass groups samples. Panel A: $\langle \cos(\theta) \rangle$ for groups in mass sample S1, computed for particles in regions with $\rho \gg \bar{\rho}$ (solid line), $\rho \sim \bar{\rho}$ (dashed line) and $\rho \ll \bar{\rho}$ (dotted line). Panel B: same as A, for groups in sample S2. Panel C: r groups in sample S3. Panel D: groups in sample S4.

for particles in low- (dotted line), intermediate- (dashed line) and high-density (solid line) regions. As can be seen, the ratio D_i is larger for low-density particles at small separations, whereas at larger scales, the trend is similar for particles in both, high and low density regions. Inspection of panel D, indicates that an important difference of three orders of magnitude can be achieved between the number of infalling to outflowing particles for high density regions. Note that this maximum occurs at a scale $\sim 50\%$ larger than that in low density regions. In high density regions, however, this difference is not so important. It should also be noticed that, although not detected in Figure 6 for the overall ratios of infalling and outflowing particles, particles in the lower density regions show a minimum in D_i at slightly (marginally) larger distances from the halo centres than the corresponding maximum in D_o .

4 CONCLUSIONS

We now summarise the main conclusions we arrived at during the series of analyses performed on the VLS simulations. We studied the peculiar velocity field around dark-matter haloes of varying masses, considering infall velocities, the *infall angle* with respect to the halo centres, and the fractions of infalling and outflowing particles. We also studied variations in these quantities as the local dark-matter particle density varies.

We now list our main results and conclusions:

- The maximum infall velocity around the most massive groups identified in the numerical simulation ($\sim 10^{15} h^{-1} M_\odot$), is $v_{inf} \sim 900$ km/s. The results for the lowest

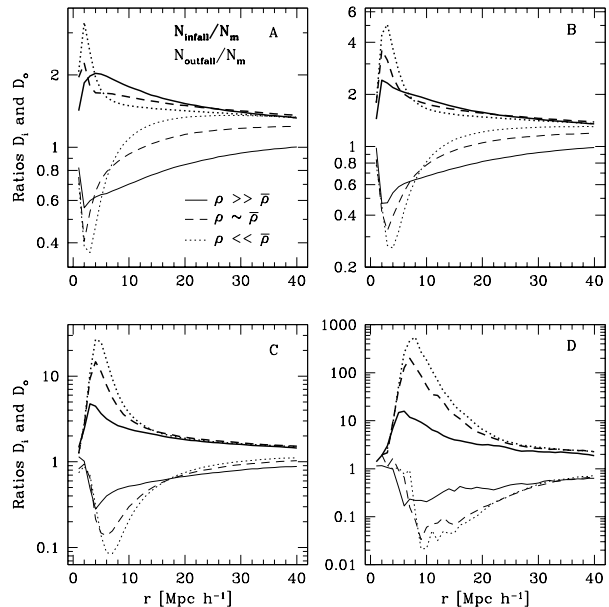


Figure 10. Dependence of $N_{outflow}/N_m$ (black) and N_{infall}/N_m (gray) with the local density of dark-matter particles, for four subsamples of halos (panels A, B, C and D for samples S1, S2, S3 and S4, respectively). Results for D_i and D_o for particles characterised by $\rho/\bar{\rho} > 2$ are shown in solid lines, whereas dashed lines shows the results for $\rho \sim \bar{\rho}$, and dotted lines the results for $\rho/\bar{\rho} < 1/2$.

mass group sample ($\sim 10^{12} h^{-1} M_\odot$) indicate a maximum infall velocity of ~ 220 km/s, decreasing very slowly at larger distances from the halo centres.

- The maximum infall velocity occurs in a narrow range of scales, $2h^{-1} \text{ Mpc} < r_{max} < 6h^{-1} \text{ Mpc}$ even when considering a broad range of group masses ($10^{12} h^{-1} M_\odot$ to $10^{15} h^{-1} M_\odot$).

- The exponential cutoff linear model analysed by Croft et al., works better for the most massive groups at small scales. It does not reproduce the infall pattern for groups samples with $M < 10^{14} h^{-1} M_\odot$, neither the large scale infall signature onto massive systems in any of our subsamples S1 to S4.

- We find a power law relation between the maximum infall velocity and mass. The Croft et al. model with an exponential overdensity cutoff provides a good fit for $\delta_c \simeq 45$.

- Large mass groups show a stronger alignment between the dark-matter particle peculiar velocity and its cluster-centric position than do low mass groups. Regardless of the halo mass, this maximum alignment occurs at intermediate scales, $2h^{-1} \text{ Mpc} < r_{max} < 8h^{-1} \text{ Mpc}$.

- There are remarkable differences between the dynamical behaviour of low- and high-density particles. In general, higher density particles exhibit higher infall velocities and lower alignment than particles in lower density environments. The difference in infall is less evident when considering high mass haloes, and the alignment becomes similar for high and low density particles for larger distances to halo centres. However, at large enough distances, high-density

particles become even more aligned than lower density particles, specially for low mass haloes.

We have also considered the possibility that substructure could affect our analysis. According to the results of Aubert, Pichon & Colombi (2004) the infall pattern of the largest halos is affected by substructure only at small scales ($r < 2Mpc$). Since the maxima occurs well beyond this scale, we are confident that our results are not likely to change under the presence of substructure.

In spite of the fact that mass flows toward clusters in an anisotropic fashion preferentially through the filamentary structure, the results provided give useful mean values of velocity flows which can be used to assess the systematic infall onto growing structures. The particular analysis performed provide direct measures of the maximum infall pattern and halo mass dependence and can be used to estimate gas dynamical processes such as ram pressure stripping that may initiate galaxy transformation in the outskirts of clusters.

ACKNOWLEDGMENTS

MP acknowledges receipt of a CONICET fellowship. NDP was supported by a Proyecto FONDECYT Postdoctoral 3040031. This work was supported in part by the "ESO Center for Astrophysics" at Catolica and by the European Commission's ALFA-II programme through its funding of the Latin-american European Network for Astrophysics and Cosmology, LENAC. The simulations in this paper were carried out by the Virgo Supercomputing Consortium using computers based at the Computing Centre of the Max-Planck Society in Garching and at the Edinburgh Parallel Computing Centre. The data are publicly available at <http://www.mpa-garching.mpg.de/NumCos>. This research has made use of NASA's Astrophysics Data System.

REFERENCES

- Aubert D., Pichon C. & Colombi S., 2004, MNRAS, 352, 344.
 Bothun G.D., West M.J., Mould J.R. & Schommer R.A., 1990, ApJ, 353, 344.
 Ceccarelli M.L., Valotto C., Padilla N., Lambas D.G., Giovanelli R. & Haynes M., 2005, ApJ, 622, 853.
 Cole S. & Lacey C., 1996, MNRAS, 281, 716.
 Croft R.A.C., Dalton G.B. & Efstathiou G., 1999, MNRAS, 305, 547.
 Davis M., Efstathiou G., Frenk C.S. & White S.D.M., 1985, ApJ, 292, 371.
 Dekel A., 1999, *Formation of Structure in the Universe*, ed. Dekel A. and Ostriker J.P. (Cambridge University Press), p. 250.
 Diaferio A., 1999, MNRAS, 309, 610.
 Diaferio A. & Geller M.J., 1997, ApJ, 481, 633.
 Einasto M., Suhhonenko I., Heinämäki P., Einasto J., & Saar E., 2005, A&A, 436, 17.
 Gunn J.E., 1978, *Observational Cosmology*, 8th Annual Saas-Fee Course, edited by A. Maeder, L. Martinet and G. Tammann (Geneva Observatory, Sauverny).
 Hioteles N., 2001, A&A, 375, 338.
 Peebles P.J.E., 1976, ApJ, 205, 318.
 Peebles P.J.E., 1980, *Large Scale Structure of the Universe* (Princeton University, Princeton).
 Regös E. & Geller M.J., 1989, ApJ, 98, 755.
 Seljak U. & Zaldarriaga M., 1996, ApJ, 469, 437.
 Shaw L., Weller J., Ostriker J.P. & Bode P., astro-ph/0509856.
 Strauss M.A. & Willick J.A., 1995, Phys. Rep., 261, 271.
 Yahil A., 1985, *The Virgo Cluster*, ed. Richter O. and Binggeli B. (ESO, Garching), p. 359.
 Yoshida N., Sheth R., & Diaferio A., 2001, MNRAS, 328, 669.